



## Dual-metal hydroxide@oxide heterojunction catalyst constructed via corrosion engineering for large-current oxygen evolution reaction

Zhong Li <sup>a</sup>, Xinglin Zhang <sup>b</sup>, Zheyen Zhang <sup>c</sup>, Peng Chen <sup>c,\*</sup>, Yizhou Zhang <sup>a,\*</sup>, Xiaochen Dong <sup>b,d,\*\*</sup>

<sup>a</sup> School of Chemistry and Materials Science, Nanjing University of Information Science & Technology, Nanjing 210044, China

<sup>b</sup> Key Laboratory of Flexible Electronics (KLOFE), Institute of Advanced Materials (IAM), Nanjing Tech University (NanjingTech), Nanjing 211816, China

<sup>c</sup> School of Chemistry, Chemical Engineering and Biotechnology, Institute for Digital Molecular Analytics and Science, Nanyang Technological University, 637457, Singapore

<sup>d</sup> School of Chemistry & Materials Science, Jiangsu Normal University, Xuzhou 221116, China



### ARTICLE INFO

#### Keywords:

Heterojunction catalysts  
Large-current OER  
Corrosion engineering  
Self-supported catalysts

### ABSTRACT

Current OER electrocatalysts are hardly applicable for industrial use, which demands high current density ( $\geq 1000 \text{ mA cm}^{-2}$ ) at low overpotential ( $\leq 300 \text{ mV}$ ) with long-term stability ( $\geq 100 \text{ h}$ ). Herein self-supported heterojunction catalyst, NiCo-OH@Ni<sub>x</sub>Fe<sub>y</sub>O<sub>4</sub> on Fe foam (FF), is in situ synthesized using two-step corrosion engineering. It only requires an overpotential 275 mV to drive the current density of 1000 mA cm<sup>-2</sup> with good long-term stability. Theoretical calculations reveal that such good performance is attributable to electron transfer from NiCo-OH to Ni<sub>x</sub>Fe<sub>y</sub>O<sub>4</sub> which weakens the adsorption energy of reaction intermediate (OOH\*) to promote the release of O<sub>2</sub> and lowers the free energy barriers for the reaction. Furthermore, a water splitting cell with NiCo-OH@Ni<sub>x</sub>Fe<sub>y</sub>O<sub>4</sub>/FF as anode and CoP@FeP/FF as cathode demonstrates its potential for industrial application. The study presents a general strategy for in situ synthesis of heterojunction catalysts on metal foams using controlled corrosion engineering for various catalytic applications.

### 1. Introduction

Hydrogen energy generated via electrochemical water splitting can be divided into two half-cell reactions, which are hydrogen evolution reaction (HER) in cathode and oxygen evolution reaction (OER) in anode [1,2]. The latter is the rate-limiting reaction because of involvement of multiple proton/electron coupled steps, thus demands efficient electrocatalysts [3]. Currently, commercially used electrocatalysts for OER are precious metal based catalysts (IrO<sub>2</sub>/RuO<sub>2</sub>) which suffer from high cost and poor stability [4,5]. Although earth-abundant transition metal-based electrocatalysts for OER have been extensively studied and demonstrated good performance at a low current density (< 100 mA cm<sup>-2</sup>), most of them work poorly at a large current density (> 500 mA cm<sup>-2</sup>) for industrial production [6,7].

Most OER electrocatalysts are synthesized in powder form, which are required to be loaded onto a conductive substrate to construct anode [8]. But the necessity for the use of binders (e.g., Nafion) compromises exposure of active sites, electron transfer, and mass transport [9].

Moreover, the powders on the electrode would be shook off by generated O<sub>2</sub> bubbles at high current density [10]. To tackle these issues, catalytically active species can be in situ grown on the conductive substrate, such as metal or alloy foam, to obtain self-supported electrocatalysts [11]. They are commonly synthesized by hydrothermal, solvothermal and electro-deposition methods [12], which often require tedious synthesis procedure and harsh reaction conditions such as high temperature ( $\geq 100^\circ\text{C}$ ), high pressure, and high voltage. To avoid these problems, self-supported electrocatalysts have been constructed at low-cost via chemical corrosion of metal foam [13–15]. For instance, when Fe Foam is immersed in NiCl aqueous solution, gradually released Fe ions will be co-precipitated with Ni ion to form NiFe-layered double hydroxide (NiFe-LDH) [16]. Ni foam can be corroded by FeCl<sub>3</sub> in ethanol to form NiFe oxyhydroxide [17]. When corrosive liquid is changed to HCl aqueous solution, the corrosion layer of NiO is obtained [18]. Although these self-supported metal oxides or (oxy)hydroxides produced by corrosion engineering are recognized as state-of-the-art OER electrocatalysts [19], they are not able to meet the expectation by fuel

\* Corresponding authors.

\*\* Corresponding author at: Key Laboratory of Flexible Electronics (KLOFE), Institute of Advanced Materials (IAM), Nanjing Tech University (NanjingTech), Nanjing 211816, China.

E-mail addresses: [chenpeng@ntu.edu.sg](mailto:chenpeng@ntu.edu.sg) (P. Chen), [yizhou.zhang@nuist.edu.cn](mailto:yizhou.zhang@nuist.edu.cn) (Y. Zhang), [iamxcdong@njtech.edu.cn](mailto:iamxcdong@njtech.edu.cn) (X. Dong).

Cells and Hydrogen Joint Undertaking in Europe (FC HJU) [20], that is, driving a current density  $\geq 800 \text{ mA cm}^{-2}$  in alkaline electrolyte at an overpotential  $\leq 300 \text{ mV}$  [21] with good long-term stability ( $\geq 100 \text{ h}$ ) [22].

It has been demonstrated that heterojunction catalysts with coupled interfaces between two active phases often offer better catalytic performance than the homogeneous counterparts [23,24]. Firstly, the lattice strain induced at heterojunction modulates local coordination environment of metal atom, leading to the upshift (tensile strain)/downshift (compressive strain) of d-band center of active sites for OER, thereby optimizing the binding energy between active sites and reaction intermediates [25]. Furthermore, the two active phases may cooperate to complete OER process and thus synergistically improve reaction kinetics [26]. Lastly, the electron transfer at heterojunction may modulate the electronic structures of the catalyst, leading to enhanced catalytic activity and optimized adsorption energy of reaction intermediates [27]. Therefore, we conceive that constructing heterojunctions between metal oxides and metal (oxy)hydroxide through corrosion engineering may be an effective strategy to realize large-current OER for industrial application.

In this work, we synthesized a dual-metal hydroxide@oxide heterojunction catalyst ( $\text{NiCo-OH}@\text{Ni}_x\text{Fe}_y\text{O}_4$ ) on Fe foam (FF) via two-step corrosion engineering. This self-supported electrocatalyst only requires a low overpotential of 275 mV to drive a large current density of 1000  $\text{mA cm}^{-2}$  with excellent long-term stability. As revealed by density functional theory (DFT) calculations, such good performance is attributable to electron transfer from  $\text{NiCo-OH}$  to  $\text{Ni}_x\text{Fe}_y\text{O}_4$ , which optimizes the adsorption of reaction intermediates because of altered electronic structure. A full water splitter cell was constructed using  $\text{NiCo-OH}@\text{Ni}_x\text{Fe}_y\text{O}_4/\text{FF}$  as anode and dual metal phosphide ( $\text{CoP}@/\text{FeP}/\text{FF}$ ) fabricated by corrosion and phosphorization as cathode. The cell only requires a voltage of 1.769 V to produce a current density of 1000  $\text{mA cm}^{-2}$  with good long-term stability.

## 2. Experimental section

### 2.1. Synthesis of CoFe-LDH/FF

Fe foam (FF) was washed by 1 mol/L of HCl, acetone and ethanol, and then dried at 60 °C under vacuum overnight. Then 8 pieces of cleaned FFs ( $1 \times 1.5 \text{ cm}^2$ ; Fig. S1), 5 mmol of  $\text{Co}(\text{NO}_3)_2 \cdot 6 \text{ H}_2\text{O}$  and 25 mmol of urea were put into 50 mL deionized (DI) water with 30 min ultrasonication to promote salt dispersion. The mixture was then transferred into 100 mL Teflon-lined autoclave and heated at 90 °C for 12 h to obtain CoFe-LDH/FF, which was subsequently washed by DI water, ethanol and dried in a vacuum oven at 60 °C.

### 2.2. Synthesis of $\text{NiCo-OH}@\text{Ni}_x\text{Fe}_y\text{O}_4/\text{FF}$

5 g of 2-methylimidazole and 4 g of triethylamine were dissolved in 20 mL DI water under ultrasonication for 30 min, CoFe-LDH/FF ( $1 \times 3 \text{ cm}^2$ ) was immersed into the mixture and heated at 75 °C for 6 h. The resulting CoFe-ZIF-67/FF was then washed by DI water, ethanol and dried in a vacuum oven at 60 °C. Subsequently, the sample ( $1.5 \times 1 \text{ cm}^2$ ) was immersed in 6 mg  $\text{mL}^{-1}$  of  $\text{Ni}(\text{NO}_3)_2$  aqueous solution with stirring at 50 °C for 2 h. The obtained  $\text{NiCo-OH}@\text{Ni}_x\text{Fe}_y\text{O}_4/\text{FF}$  was washed by DI water, ethanol and dried at 60 °C under vacuum overnight.

### 2.3. Synthesis of $\text{CoP}@/\text{FeP}/\text{FF}$

CoFe-LDH/FF ( $1 \times 3 \text{ cm}^2$ ) was placed downstream inside a tube furnace while 6 mmol of  $\text{NaH}_2\text{PO}_2 \cdot \text{H}_2\text{O}$  was placed upstream. Phosphorization to produce  $\text{CoP}@/\text{FeP}/\text{FF}$  was realized by heating to 300 °C with a rate of  $2 \text{ }^\circ\text{C min}^{-1}$  and maintaining at this temperature for 2 h under Ar atmosphere.

## 2.4. Characterization

X-ray diffraction (XRD) patterns were recognized via a SmartLab diffractometer (Smartlab3KW, Rigaku) with a scanning rate of  $10^\circ \text{ min}^{-1}$ , the powders used for the test were sonicated from the self-supported catalyst. The morphology and element distribution were recorded by scanning electron microscope (FEI-Scios 2 Hivac). The crystal parameters were measured through high resolution transmission electron microscopy (FEITecnai G2 F30). XPS data were measured via a Thermo Scientific K-Alpha+ spectroscopy. The Raman spectra were measured on a Renishaw inVia Reflex Raman spectrometer (under an excitation of 632 nm laser).

## 2.5. Electrochemistry

All electrochemical tests were conducted on an electrochemical workstation (CHI 660D) with a standard three-electrode system at 25 °C unless otherwise specified. For HER and OER tests, self-supported catalysts served as the work electrodes (WE; working area of  $0.5 \times 0.5 \text{ cm}^2$ , the rest area was sealed with epoxy resin), Ag/AgCl (3.5 M KCl, 0.2046 V vs normal hydrogen electrode) was used as the reference electrode (RE), and graphite rod was used as the counter electrodes (CE).  $\text{NiCo-OH}@\text{Ni}_x\text{Fe}_y\text{O}_4/\text{FF}$  and  $\text{CoP}@/\text{FeP}/\text{FF}$  were utilized as the anode and cathode respectively to construct a two-electrode system for overall water splitting. For comparison, water splitting cell based on commercial catalysts were prepared by dropping  $\text{RuO}_2$  (Pt/C) inks (490  $\mu\text{L}$  DI water, 490  $\mu\text{L}$  ethanol, 20  $\mu\text{L}$  5 wt% Nafion solution and 5 mg  $\text{RuO}_2$  (anode) or Pt/C (cathode) powders on clean Fe Foam ( $1 \times 1 \text{ cm}^2$ ) and dried overnight at 60 °C under vacuum. 1 M KOH aqueous solution (pH=13.6) was used as electrolyte, and the potentials vs reversible hydrogen electrode (RHE) was calculated from the measured potentials according to Eq. 1 [28]:

$$E(\text{vs RHE}) = E(\text{vs Ag/AgCl}) + 0.2046 + 0.059 \times pH \quad (1)$$

Forward and reverse polarization curves were obtained at a scan rate of  $1 \text{ mV s}^{-1}$  (forward polarization curves were shown in Fig. S2), and the corresponding Tafel slopes were calculated following the Eq. 2 [28]:

$$\eta = b \log|j| + a \quad (2)$$

where  $\eta$  is overpotential,  $b$  is Tafel slope,  $j$  is current density.

Cyclic voltammetry (CV) method was utilized to calculate double-layer capacitances ( $C_{dl}$ ) in non-faradaic region. The scan rates of CV curves were set to 2, 4, 6, 8 and  $10 \text{ mV s}^{-1}$  respectively. The electrochemically active surface area (ESCA) was then calculated via Eq. 3 [29]:

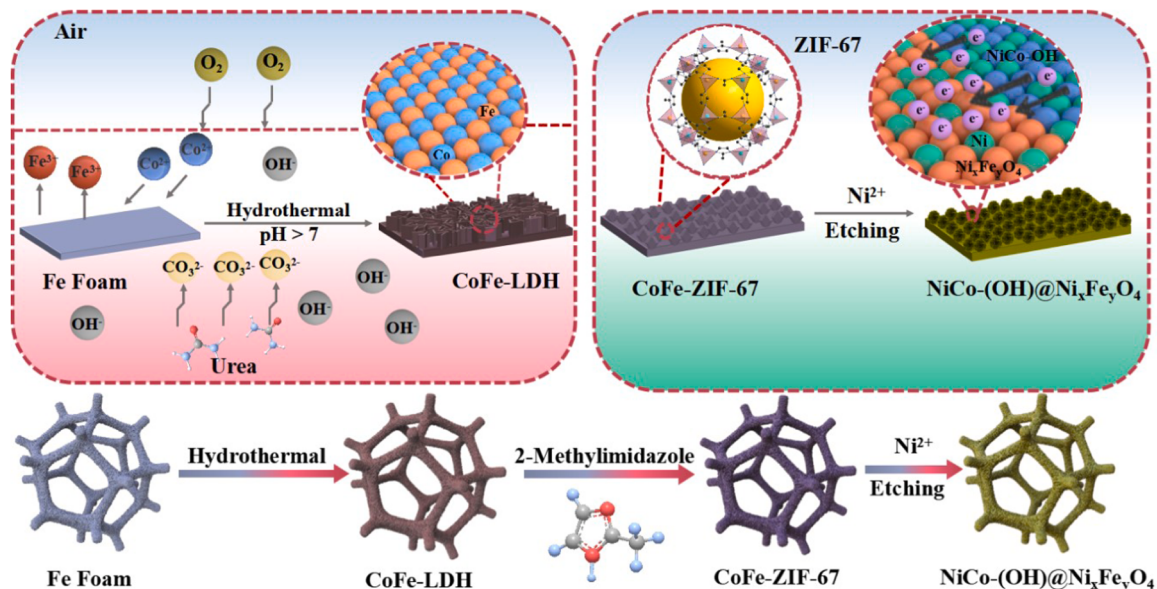
$$ECSCA = \frac{C_{dl}}{C_s} \times S_A \quad (3)$$

where  $C_s$  is specific capacitance of electrocatalysts ( $0.04 \text{ mF cm}^{-2}$ ),  $S_A$  is actual surface area.

Faraday efficiency (FE) of cathode and anode in overall water splitting cell were calculated by drainage method. The water splitting was performed in a H-type electrolytic cell with the current of 0.25 A at 20 °C. The cathode and anode were separated by a proton exchange membrane to prevent the diffusion of  $\text{H}_2$  and  $\text{O}_2$  to the opposite electrode. The generated  $\text{H}_2$  and  $\text{O}_2$  were collected in methyl orange solution filled in cylinder (methyl orange was used to mark the cylinder scale). The time required for unit amount of  $\text{H}_2$  and  $\text{O}_2$  evolution (10 mL for  $\text{H}_2$  and 5 mL for  $\text{O}_2$ ) was recorded and the FE was calculated as follows [30]:

$$FE = \frac{znF}{It} \quad (4)$$

where  $z$  is electron transfer number (for  $\text{H}_2$ ,  $z = 4$ ; for  $\text{O}_2$ ,  $z = 2$ ),  $n$  is the molar amount of generated gas (mol),  $F$  is Faraday constant



**Scheme 1.** Illustration for synthesis of NiCo-OH@Ni<sub>x</sub>Fe<sub>y</sub>O<sub>4</sub> heterojunction catalyst on Fe foam as a self-supported anode for OER.

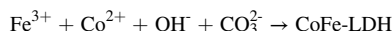
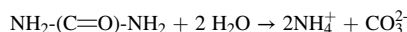
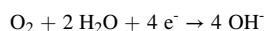
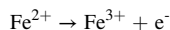
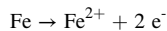
(96485 C mol<sup>-1</sup>), I is test current (A) and t is test time (s).

Stability of the samples was examined through 2000 cycles of CV with a scan rate of 50 mV s<sup>-1</sup> and chronopotentiometric measurements at the current density of 1000 mA cm<sup>-2</sup>. iR compensation was utilized to correct original linear sweep voltammetry (LSV, Fig. S3) and chronopotentiometric curves of samples ( $E = E_{\text{initial}} - i \times R_s$ , where  $i$  is current,  $R_s$  is solution resistance obtained from EIS and shown in Table S1).

### 3. Results and discussion

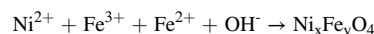
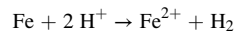
#### 3.1. Synthesis of NiCo-OH@Ni<sub>x</sub>Fe<sub>y</sub>O<sub>4</sub> heterojunction catalyst

The synthesis of NiCo-OH@Ni<sub>x</sub>Fe<sub>y</sub>O<sub>4</sub> heterojunction catalyst is illustrated in Scheme 1, which involves two-step corrosion. Co-LDH was synthesized under mild hydrothermal condition (90 °C) in the presence of urea and Co<sup>2+</sup> ions. The temperature is lower than that for typical hydrothermal syntheses to allow energy saving, yet it is high enough to decompose urea [31]. Urea as a weak Brønsted base was hydrolyzed to ammonium carbonate ((NH<sub>4</sub>)<sub>2</sub>CO<sub>3</sub>), providing CO<sub>3</sub><sup>2-</sup> ions and alkaline condition for precipitation of Co-based hydroxide [32]. CO<sub>3</sub><sup>2-</sup> ions intercalated between the hydroxide layers to form hydrotalcite-like LDH. Hydrothermal condition also enhanced the corrosion of Fe foam (Fig. S4a) by H<sub>2</sub>O and oxygen whereby releasing abundant Fe<sup>3+</sup> ions, which precipitate together Co<sup>2+</sup> ions to form CoFe-LDH on the surface of Fe foam [29]. The formation of CoFe-LDH was confirmed by scanning electron microscopy (SEM) which revealed its morphology of microsized thin sheet, and by energy dispersive X-ray (EDX) mapping which indicated the uniform distribution of Co, Fe and O elements (Fig. S5). The chemical reactions involved in the abovementioned first step of corrosion are given as:



To further enhance the OER activity, the second corrosion was used to restructure CoFe-LDH to NiCo-OH@Ni<sub>x</sub>Fe<sub>y</sub>O<sub>4</sub> heterojunction catalyst. Specifically, LDH was hydrothermally transformed into zeolitic

imidazolate framework in the presence of organic ligand 2-methylimidazole (HMe-Im) and its de-protonation agent triethylamine (TEA), leading to the formation of polyhedral CoFe-ZIF-67 particles with a size of 1–2 μm (Fig. S4b). During this process, the CO<sub>3</sub><sup>2-</sup> enlarged interlayer spacing of CoFe hydroxide allowed diffusion-in of HMe-Im, H<sup>+</sup> and H<sub>2</sub>O, causing breakage of metal-hydroxide bonds (CoFe-OH) [33]. Subsequently, coordination bonding between the released ions (Co<sup>2+</sup>, Fe<sup>3+</sup>) and HMe-Im led to formation of CoFe-ZIF-67, which was then used as the template to form a hydroxide/oxide heterostructure (NiCo-OH@Ni<sub>x</sub>Fe<sub>y</sub>O<sub>4</sub>). In this step, the protons generated from hydrolysis of nickel nitrate gradually etched CoFe-ZIF-67 to release Co and Fe ions [34]. Ni ions co-precipitated with Co ions to form NiCo-hydroxide. Given the extremely low solubility of both Co(OH)<sub>2</sub> and Ni(OH)<sub>2</sub> in weak acid solution [35,36], NiCo-OH will not be etched in Ni(NO<sub>3</sub>)<sub>2</sub> solution (pH=5.8). Simultaneously, Fe Foam is corroded to release Fe<sup>2+</sup> [37]. Then Fe<sup>2+</sup> and Fe<sup>3+</sup> co-precipitated with Ni<sup>2+</sup> into Ni<sub>x</sub>Fe<sub>y</sub>O<sub>4</sub> (as shown below) [38], leading to the formation of heterojunction with NiCo-OH:



EDX mapping of NiCo-OH@Ni<sub>x</sub>Fe<sub>y</sub>O<sub>4</sub> doesn't show existence of C and N (Fig. S4c), suggesting that CoFe-ZIF-67 fully transform to NiCo-OH@Ni<sub>x</sub>Fe<sub>y</sub>O<sub>4</sub>.

#### 3.2. Characterizations

As uncovered by SEM, nanoflowers (1–2 μm) assembled by NiCo-OH@Ni<sub>x</sub>Fe<sub>y</sub>O<sub>4</sub> nanosheets were finally obtained via two step corrosion (Fig. 1a). EDX mapping shows uniform distribution of Ni, Co, Fe and O on the FF surface (Fig. 1b, c), indicating that Ni was equally incorporated into both Co and Fe phases. Further, high-resolution transmission electron microscopy (HRTEM) revealed the clear interface between the hydroxide and oxide phases and resolved the lattice fringe spacings of 0.25, 0.21 and 0.24 nm corresponding to (3 1 1) and (4 0 0) facets of Ni<sub>x</sub>Fe<sub>y</sub>O<sub>4</sub> and (0 1 1) facet of NiCo-OH respectively (Fig. 1d-g and Fig. S6).

X-ray diffraction (XRD) patterns were obtained from the powders scrapped from FF by sonication. As shown in Fig. S7, the peaks at 11.7, 23.6, 34.2, 38.8, 43.1, 46.6 and 60.7° correspond to (0 0 3), (0 0 6), (0 1 2), (0 1 5), (1 0 7), (0 1 8) and (1 1 3) planes of CoFe-LDH obtained from

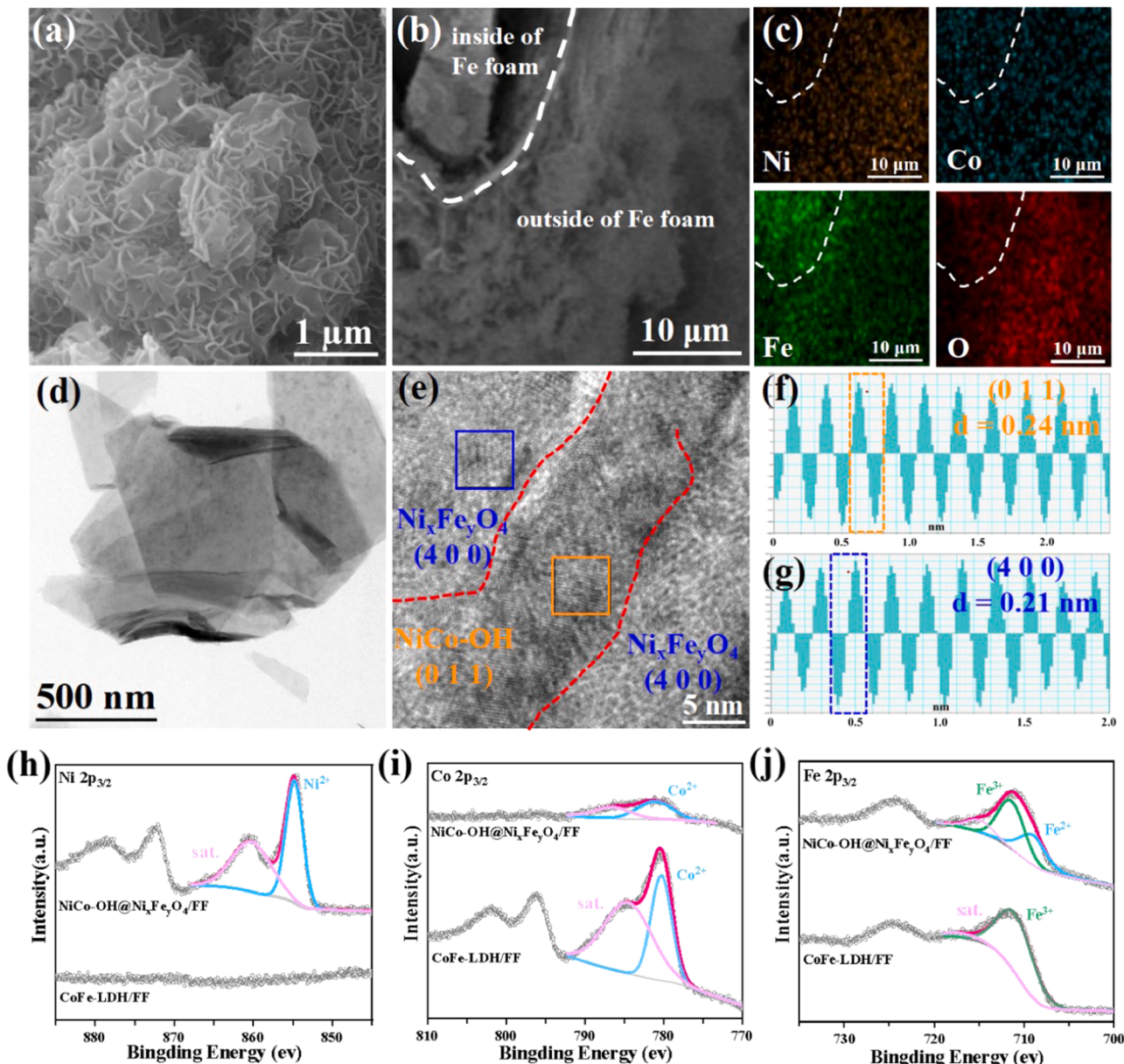


**Fig. 1.** Characterizations of NiCo-OH@Ni<sub>x</sub>Fe<sub>y</sub>O<sub>4</sub>. (a) SEM image with high magnification. (b) SEM image with low magnification of the selected area for EDX element mapping. (c) Corresponding elemental mapping of Ni, Co, Fe, and O. (d) TEM image. (e) HRTEM image (red dash lines indicate the interface between two phase). (f, g) Line scan of inverse fast Fourier transform (FFT) of (0 1 1) facets of NiCo-OH and (4 0 0) facets of Ni<sub>x</sub>Fe<sub>y</sub>O<sub>4</sub>. (h) Ni 2p XPS spectrum. (i) Co 2p XPS spectrum. (j) Fe 2p XPS spectrum.

the first corrosion step, matching well with the hydrotalcite CoFe-LDH reference (PDF #00-050-0235) [39]. The observed small peaks can be indexed to Fe<sub>3</sub>O<sub>4</sub> (PDF #97-003-1157), which are resulted from the oxidized FF surface. For NiCo-OH@Ni<sub>x</sub>Fe<sub>y</sub>O<sub>4</sub> obtained after the second corrosion, the characteristic peaks from CoFe-LDH are almost invisible whereas the peaks at 19.1° and 38.1° arise from (0 0 1) and (0 1 1) planes of β phase NiCo-OH (Fig. S8a) [40]. The peaks from (0 0 1) and (0 1 1) planes for β-Co(OH)<sub>2</sub> are located at 19.0 and 37.9° (PDF#97-008-8940), whereas that for β-Ni(OH)<sub>2</sub> are located at 19.2 and 38.6° (XRD PDF#97-002-8101). For our heterojunction catalyst (NiCo-OH@Ni<sub>x</sub>Fe<sub>y</sub>O<sub>4</sub>), the peaks lie between the characteristic peaks from β-Co(OH)<sub>2</sub> and β-Ni(OH)<sub>2</sub>. This confirms that both Ni and Co are incorporated into the hydroxide phase, i.e., forming NiCo-OH. Incorporation of Fe into Co or Ni hydroxide would transform them from β-phase to LDH phase [41,42]. Absence of the characteristic peak of LDH suggests that Fe is not incorporated into NiCo-OH. During the second

corrosion, Fe<sup>3+</sup>, Fe<sup>2+</sup> and Ni<sup>2+</sup> coprecipitated into FeNi hydroxide, which then turned into Ni<sub>x</sub>Fe<sub>y</sub>O<sub>4</sub> under heating [41]. This notion is consistent to a previous study which synthesized NiFe<sub>2</sub>O<sub>4</sub> by co-precipitation method via corrosion engineering [43]. In the XRD spectrum of our catalyst (NiCo-OH@Ni<sub>x</sub>Fe<sub>y</sub>O<sub>4</sub>), the prominent peaks at 30.1, 35.5, 43.0, 57.0 and 62.6° can be indexed to (2 2 0), (3 1 1), (4 0 0), (5 1 1) and (4 4 0) planes of Ni<sub>x</sub>Fe<sub>y</sub>O<sub>4</sub> (PDF #97-008-4102). No peaks corresponding to FeOOH (including α, β, γ and δ phase) [44,45] are observed (Fig. S8b), confirming that FeOOH was not generated during the corrosion process. Compared to CoFe-LDH/FF, the full width at half maxima (FWHM) of NiCo-OH@Ni<sub>x</sub>Fe<sub>y</sub>O<sub>4</sub>/FF is wider, indicating decreased crystallinity. This is advantageous for OER because of more catalytically active vacancy defects, unsaturated coordination bonds, and interfaces between crystalline domains [46]. Consistent with XRD, the Raman bands located around 450 and 515 cm<sup>-1</sup> correspond to the typical NiCo hydroxide phase [47], whereas the peaks at about 195, 310,

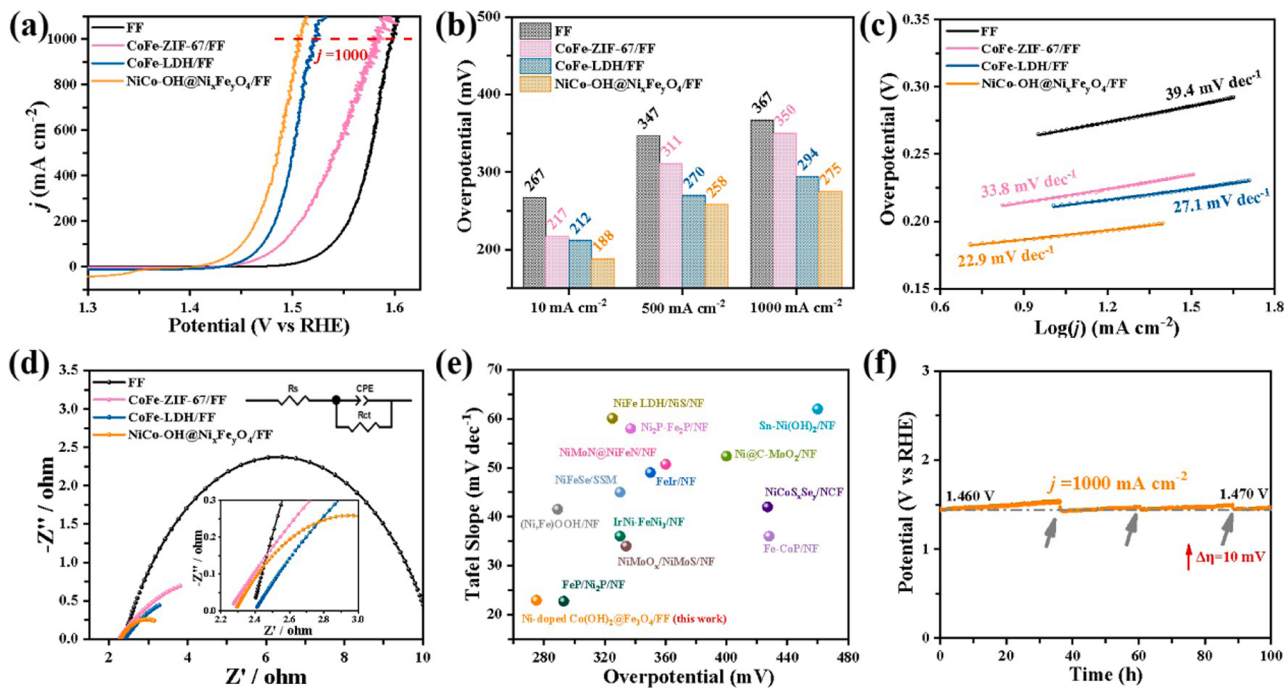


**Fig. 2.** OER performance of FF, CoFe-ZIF-67/FF, CoFe-LDH/FF, and NiCo-OH@Ni<sub>x</sub>Fe<sub>y</sub>O<sub>4</sub>/FF. (a) Reverse polarization curves. (b) Overpotentials at 10, 500 and 1000 mA cm<sup>-2</sup>. (c) Tafel plots. (d) Electrochemical impedance spectra curves at 0.5 V. Insert shows the equivalent circuit. (e) Comparison of the Tafel slopes and overpotentials at current densities of 1000 mA cm<sup>-2</sup> with other self-supported electrocatalysts. (f) The chronopotentiometric curve of NiCo-OH@Ni<sub>x</sub>Fe<sub>y</sub>O<sub>4</sub>/FF at a constant current density of 1000 mA cm<sup>-2</sup> (arrows indicate replacement with fresh 1 M KOH electrolyte).

480, 550 and 670 cm<sup>-1</sup> are assigned to T<sub>2g</sub><sup>1</sup>, E<sub>g</sub>, T<sub>2g</sub><sup>2</sup>, T<sub>2g</sub><sup>3</sup> and A<sub>1g</sub> phonon modes of Ni<sub>x</sub>Fe<sub>y</sub>O<sub>4</sub> (Fig. S8c) [48]. Taken together, heterojunction catalyst (NiCo-OH@Ni<sub>x</sub>Fe<sub>y</sub>O<sub>4</sub>/FF), instead of a mixture of trimetallic hydroxide and oxide, was obtained.

Ni 2p<sub>3/2</sub> peak at 854.76 eV (corresponding to Ni<sup>2+</sup>) appears in the X-ray photoelectron spectroscopy (XPS) spectrum of NiCo-OH@Ni<sub>x</sub>Fe<sub>y</sub>O<sub>4</sub>/FF (but not CoFe-LDH/FF) [49], which confirmed successful incorporation of Ni (Fig. 1h and Fig. S9). For CoFe-LDH, Co 2p<sub>3/2</sub> peak at 780.38 eV can be indexed to Co<sup>2+</sup> peaks [50,51], and Fe 2p<sub>3/2</sub> peak at 711.38 eV suggests the existence of Fe<sup>3+</sup> [50]. For NiCo-OH@Ni<sub>x</sub>Fe<sub>y</sub>O<sub>4</sub> heterojunction catalyst, the binding energy of Co<sup>2+</sup> upshifts to 781.12 eV probably due to electron transfer at the interface (Fig. 1i), whereas the binding energy of Fe downshifts to 710.69 eV which can be split into Fe<sup>2+</sup> and Fe<sup>3+</sup> peaks originated from Ni<sub>x</sub>Fe<sub>y</sub>O<sub>4</sub> (Fig. 1j) [52].

### 3.3. Performance of oxygen evolution reaction

We then investigated the OER performance of the synthesized catalysts using a three-electrode system in 1 M KOH solution at 25 °C. The reverse polarization curves were used to determine the overpotential in order to avoid overestimation of the catalytic activity due to the strong oxidation peak from metal species in polarization curves. As shown in Fig. 2a and b, pure FF exhibits the lowest electrocatalytic activity. Specifically, overpotentials of 267 and 367 mV are required to drive the current density of 10 and 1000 mA cm<sup>-2</sup> ( $j_{10}$  and  $j_{1000}$ ) respectively. For NiCo-OH@Ni<sub>x</sub>Fe<sub>y</sub>O<sub>4</sub>/FF, the overpotentials at  $j_{10}$  and  $j_{1000}$  are only 188 and 275 mV, which are lower than that of CoFe-ZIF-67/FF (217 mV at  $j_{10}$ , 350 mV at  $j_{1000}$ ) and CoFe-LDH/FF (212 mV at  $j_{10}$ , 294 mV at  $j_{1000}$ ). NiCo-OH@Ni<sub>x</sub>Fe<sub>y</sub>O<sub>4</sub>/FF also offers lower Tafel slope (22.9 mV dec<sup>-1</sup>) than that of CoFe-ZIF-67/FF (33.8 mV dec<sup>-1</sup>) and CoFe-LDH/FF (27.1 mV dec<sup>-1</sup>), indicating the fast catalytic kinetics and that the rate determining step (RDS) is conversion of O<sup>\*</sup> to OOH<sup>\*</sup> (Fig. 2c) [53,54]. The electrochemical surface areas (ECSA, Table S2) were calculated from double-layer capacitance ( $C_{dl}$ ) (Fig. S10) derived from cyclic voltammetry (CV) in non-Faradaic region (Fig. S11). Although

NiCo-OH@Ni<sub>x</sub>Fe<sub>y</sub>O<sub>4</sub>/FF has a smaller ECSA than CoFe-LDH/FF (378 vs. 383 cm<sup>2</sup>), its intrinsic catalytical activity, which is evidenced by reverse polarization curve normalized by ECSA [55], is higher than CoFe-LDH/FF and FF, i.e., it requires a much smaller potential to drive the same current density (Fig. S12). Fitting the Nyquist plots obtained from electrochemical impedance spectroscopy (Fig. 2d) gives the charge-transfer resistance ( $R_{ct}$ ) (Table S3). NiCo-OH@Ni<sub>x</sub>Fe<sub>y</sub>O<sub>4</sub>/FF gives a much lower  $R_{ct}$  (1.34 Ω) than that of CoFe-LDH/FF, CoFe-ZIF-67/FF and FF (3.15, 4.67 and 7.90 Ω), suggesting the fast charge transfer rate. Taken together, the excellent OER performance of NiCo-OH@Ni<sub>x</sub>Fe<sub>y</sub>O<sub>4</sub>/FF is attributable to its high intrinsic catalytic activity, fast OER kinetics, and low charge transfer resistance. It outperforms previously reported self-supported OER electrocatalysts (Fig. 2e, Table S4).

Furthermore, NiCo-OH@Ni<sub>x</sub>Fe<sub>y</sub>O<sub>4</sub>/FF shows excellent long-term stability at large current density. Specifically, during the chronopotentiometric measurement for 100 h, the overpotential of NiCo-OH@Ni<sub>x</sub>Fe<sub>y</sub>O<sub>4</sub>/FF only increased by 10 mV at  $j_{1000}$  (Fig. 2f). In addition, after 2000 cycles of CV (peak current density >1000 mA cm<sup>-2</sup>) with the scan rate of 50 mV s<sup>-1</sup>, the overpotentials at  $j_{10}$  and  $j_{1000}$ , Tafel slope,  $C_{dl}$  and  $R_{ct}$  remained steady (Fig. S13). Although agglomeration of NiCo-OH@Ni<sub>x</sub>Fe<sub>y</sub>O<sub>4</sub> nanosheets occurred after OER (Fig. S14a), the catalyst still preserved uniform distributions of all elements (Fig. S14b, c), crystalline facets of Ni<sub>x</sub>Fe<sub>y</sub>O<sub>4</sub> and NiCo-OH, and heterojunction structure, e.g., interface between (4 0 0) plane of Ni<sub>x</sub>Fe<sub>y</sub>O<sub>4</sub> (0.21 nm) and (1 0 0) plane of NiCo-OH (0.27 nm) (Fig. S14d-l). Furthermore, the characteristic peaks in XRD and Raman spectrum were not shifted (Fig. S8). The XPS spectra of NiCo-OH@Ni<sub>x</sub>Fe<sub>y</sub>O<sub>4</sub>/FF before and after long-term operation are similar (Fig. S15). The outstanding stability at high current densities suggests the potential of NiCo-OH@Ni<sub>x</sub>Fe<sub>y</sub>O<sub>4</sub>/FF for industrial application.

### 3.4. Density function theory calculation for oxygen evolution reaction

The density functional theory (DFT) calculation was utilized to

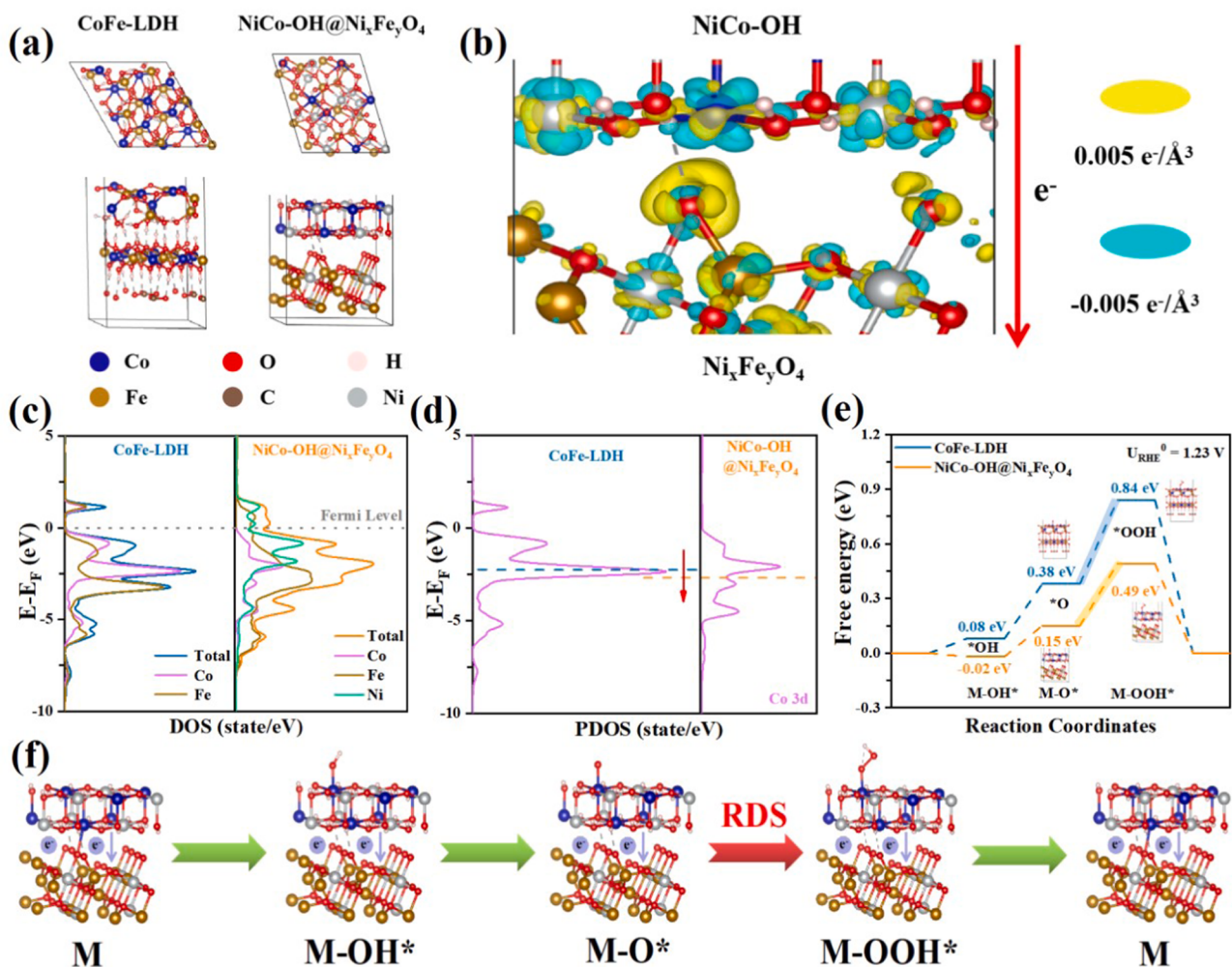


**Fig. 3.** DFT calculations. (a) Top and side views of CoFe-LDH and NiCo-OH@Ni<sub>x</sub>Fe<sub>y</sub>O<sub>4</sub>. (b) Charge density difference at the interface of NiCo-OH and Ni<sub>x</sub>Fe<sub>y</sub>O<sub>4</sub>. Cyan and yellow indicate electron depletion and accumulation, respectively. (c) Density of states (DOS). (d) Partial density of states (PDOS) of Co. (e) Free energy diagrams for OER of CoFe-LDH and NiCo-OH@Ni<sub>x</sub>Fe<sub>y</sub>O<sub>4</sub> and (f) OER reaction pathways of NiCo-OH@Ni<sub>x</sub>Fe<sub>y</sub>O<sub>4</sub>.

reveal the mechanisms underlying the superior OER performance of NiCo-OH@Ni<sub>x</sub>Fe<sub>y</sub>O<sub>4</sub>/FF (Fig. 3). According to the atomic ratio from XPS (Table S5), we constructed CoFe-LDH (Co:Fe = 1:1) model and NiCo-OH@Ni<sub>x</sub>Fe<sub>y</sub>O<sub>4</sub> (Co:Fe:Ni = 1:3:2) model (Fig. 3a). For NiCo-OH@Ni<sub>x</sub>Fe<sub>y</sub>O<sub>4</sub>, the Ni was equally incorporated into both Co and Fe phases. As shown by charge density differences analysis (Fig. 3b), there is electron transfer from NiCo-OH to Ni<sub>x</sub>Fe<sub>y</sub>O<sub>4</sub> due to the strong electronic coupling effect at the interface [56]. It has been shown that electron-deficient NiCo-OH is favorable for adsorption of oxygen intermediates in OER [57]. Additionally, it has been observed from metal-hydroxide based heterojunction catalysts (NiFe-LDH/Co<sub>3</sub>O<sub>4</sub> [58] and MoS<sub>2</sub>/NiFe-LDH heterojunction [59]) that hydroxide phase transfers electrons to oxide or sulfide phase and the electron-deficient hydroxide phase serves as the active site for adsorption of reaction intermediates. Therefore, NiCo-OH in our heterojunction catalyst should be the active phase. The electronic configuration of Co ( $t_{2g}^5 e_g^1$ ) and its oxidation to high-valence species (Co<sup>3+</sup> or Co<sup>4+</sup>) at anode are beneficial to OER [60]. Therefore, Co species are usually the catalytical centers. As demonstrated previously [61], incorporation of Ni into Co(OH)<sub>2</sub> causes a valence increase of Co<sup>2+</sup> as shown by specific Bader charge analysis, which is beneficial to adsorption of the first O intermediate (OH<sup>\*</sup>). Consistently, the 2p<sub>3/2</sub> XPS peak of Co<sup>2+</sup> shifted to higher binding energy after Ni-incorporation. Similar upshift was observed in our catalyst NiCo-OH@Ni<sub>x</sub>Fe<sub>y</sub>O<sub>4</sub> (Fig. 1i). Thus, electron-deficient Co<sup>2+</sup> in NiCo-OH active phase is the active site. Furthermore, as shown in Fig. S16, CV peak of

NiCo-OH@Ni<sub>x</sub>Fe<sub>y</sub>O<sub>4</sub>/FF around 1.25 V vs RHE is attributable to the oxidation of Co<sup>2+</sup> to Co<sup>3+</sup>, whereas the peak around 1.45 V vs RHE indicates oxidation of Co<sup>3+</sup> to Co<sup>4+</sup> [61,62], indicating that the Co<sup>2+</sup> sites is oxidized to high valence before oxygen evolution occurs. These oxidation peaks are negatively shifted as compared to that of CoFe-LDH, indicating that incorporated Ni lowers the energy barrier of oxidization of Co<sup>2+</sup> whereby accelerating catalytic kinetics. In addition, for NiCo-OH@Ni<sub>x</sub>Fe<sub>y</sub>O<sub>4</sub>, there was no shift in the binding energy of Ni 2p<sub>3/2</sub> after OER, whereas the binding energies of Fe 2p<sub>3/2</sub> and Co 2p<sub>3/2</sub> had a negative shift of 0.68 eV and a positive shift of 0.57 eV respectively (Fig. S15). The electron transfer is stronger than that of CoFe-LDH, indicating incorporated Ni accelerates the electron transfer from Co to Fe species. Taken together, for NiCo-OH@Ni<sub>x</sub>Fe<sub>y</sub>O<sub>4</sub>/FF, Co in NiCo-OH phase is the active adsorption site (Fig. S17a) and Ni promotes the conversion of Co<sup>2+</sup> to high-valence-states to enhance OER. For CoFe-hydroxide, the previous DFT investigation suggested that Fe facilitates the transition of Co<sup>2+</sup> to higher valence state, and Co site offered a smaller overpotential for OER than that of Fe site as evidenced by the theoretical volcano plot [63]. Therefore, Co should be the active site rather than Fe in CoFe-LDH (Fig. S17b).

As demonstrated in Fig. 3c, carrier density of NiCo-OH@Ni<sub>x</sub>Fe<sub>y</sub>O<sub>4</sub> around Fermi Level is higher than that of CoFe-LDH, indicating the higher conductivity of NiCo-OH@Ni<sub>x</sub>Fe<sub>y</sub>O<sub>4</sub> which is beneficial for OER [57]. Further, according to d-band center theory [64], anti-bonding states are generated from the coupling between d-orbitals of the metal

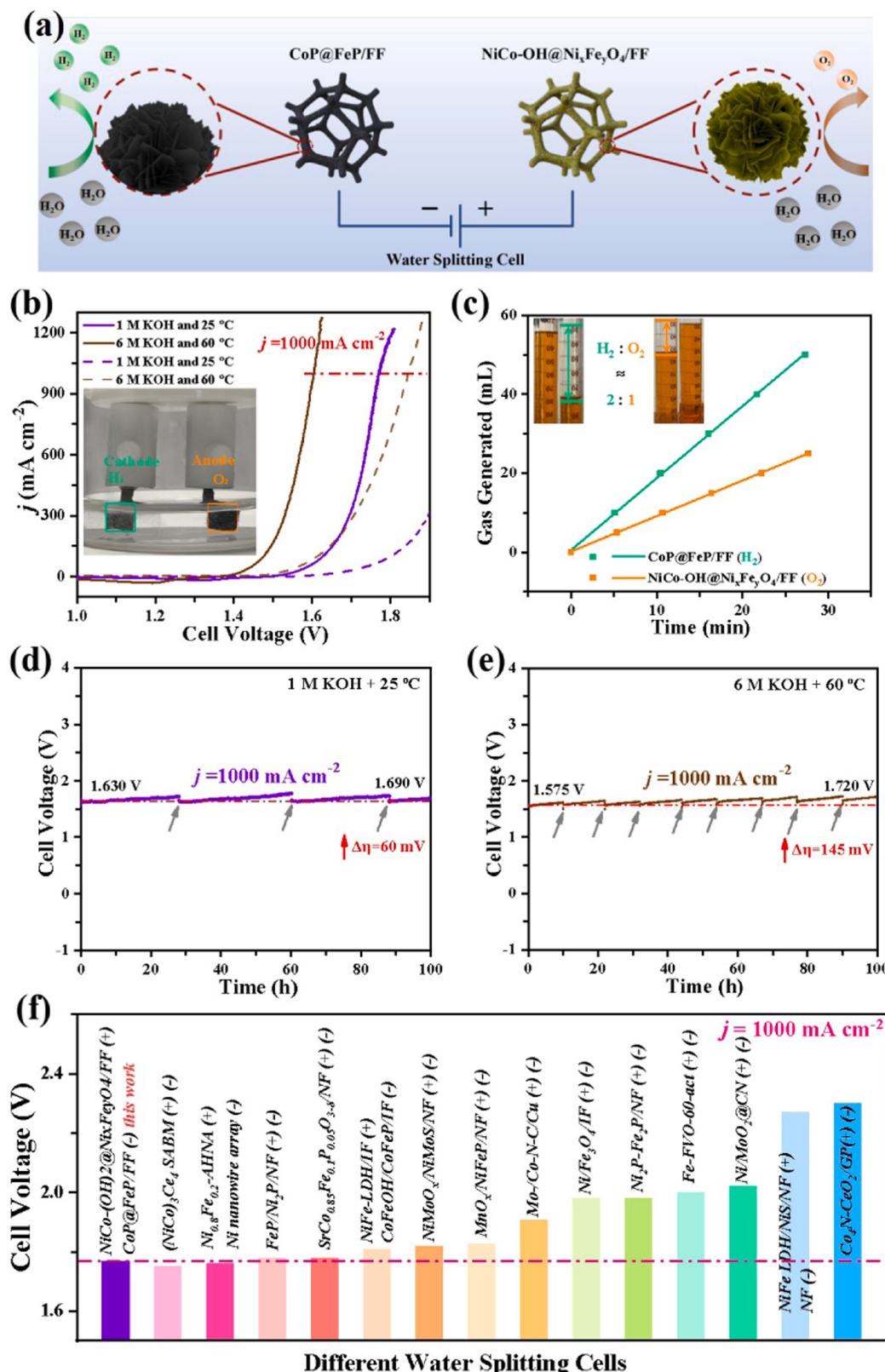


**Fig. 4.** Overall water splitting cell with NiCo-OH@Ni<sub>x</sub>Fe<sub>y</sub>O<sub>4</sub>/FF as anode and CoP@FeP/FF as cathode. (a) Scheme of NiCo-OH@Ni<sub>x</sub>Fe<sub>y</sub>O<sub>4</sub>/FF (+) || CoP@FeP/FF (-) water splitting cell. (b) Reverse polarization curves of cells in 1 M KOH at 25 °C and in 6 M KOH at 60 °C (solid line: NiCo-OH@Ni<sub>x</sub>Fe<sub>y</sub>O<sub>4</sub>/FF (+) || CoP@FeP/FF (-), dotted line: RuO<sub>2</sub> (+) || Pt/C (-)). Inset shows generation of H<sub>2</sub> and O<sub>2</sub> bubbles on cathode and anode. (c) H<sub>2</sub> (green line) and O<sub>2</sub> (orange line) over time. Insert shows that the generated H<sub>2</sub> and O<sub>2</sub> are 50 mL and 25 mL respectively. (d) Chronopotentiometric measurement for 100 h at the constant current density of 1000 mA cm<sup>-2</sup> in 1 M KOH and 25 °C (arrows indicate replacement with fresh 1 M KOH electrolyte). (e) Chronopotentiometric measurement for 100 h at the constant current density of 1000 mA cm<sup>-2</sup> in 6 M KOH and 60 °C (arrows indicate replacement with fresh 6 M KOH electrolyte). (f) Comparison of the cell voltage with the reported electrocatalysts in 1 M KOH.

atom and 2p-orbitals of O atom, and downshift of the d-band center of the metal atom indicates a decrease of anti-bonding energy and more filled electrons, which weaken the metal-O bonding. Thus, the observed downshift of d-band center ( $\epsilon_d$ ) of Co in NiCo-OH@Ni<sub>x</sub>Fe<sub>y</sub>O<sub>4</sub> as compared to that of CoFe-LDH suggests the lower binding energy of OOH\* on Co sites (Fig. 3d), which facilitates the release of O<sub>2</sub> and promotes OER kinetics [65]. Moreover, the Gibbs free energy ( $\Delta G$ ) for each reaction step during OER is lower on NiCo-OH@Ni<sub>x</sub>Fe<sub>y</sub>O<sub>4</sub> (Fig. 3e, f), particularly,  $\Delta G$  for the RDS, i.e., the conversion of O\* to OOH\* (0.34 vs. 0.46 eV).

To sum up, the excellent OER performance of NiCo-OH@Ni<sub>x</sub>Fe<sub>y</sub>O<sub>4</sub>/FF is attributable to the following reasons: 1) abundant loading of the catalysts, 3D conductive network, and unhindered mass transport enabled by FF; 2) in situ growth of catalyst allows stable anchoring and seamless electronic coupling with the current collector; 3) low charge-transfer resistance; 4) charge transfer from NiCo-OH to Ni<sub>x</sub>Fe<sub>y</sub>O<sub>4</sub> at the heterojunction optimizes the binding energy of the reaction intermediates and lowers the free energies for all the reaction steps, particularly the RDS.

### 3.5. Performance of hydrogen evolution reaction and overall water splitting

Considering the outstanding OER performance, we utilized NiCo-OH@Ni<sub>x</sub>Fe<sub>y</sub>O<sub>4</sub>/FF as the anode to construct an electrolytic cell for overall water splitting. Similar to the construction of anode, a self-supported cathode was simply fabricated by phosphation of CoFe-LDH/FF to produce CoP@FeP/FF. It has been demonstrated that metal-phosphides exhibit high hydrogen evolution reaction (HER) activity [66,67]. The XRD, SEM, and EDX mapping of CoP@FeP/FF are shown in Fig. S18. As seen, CoP@FeP/FF maintained the same thin micro-sheet morphology as CoFe-LDH/FF, and P element is uniformly dispersed. The XRD pattern of CoP@FeP/FF presents the characteristic peaks from CoP (PDF#97-004-3249) and FeP (PDF#97-001-5057). As shown in Fig. S19, the overpotential at  $j_{1000}$ ,  $C_{dl}$ , and  $R_{ct}$  are 280 mV, 319.6 mF cm<sup>-2</sup> and 3.85 Ω respectively. The Tafel slope of CoP@FeP/FF for HER is 139.6 mV dec<sup>-1</sup>, indicating that the reaction is dominated by Volmer-Heyrovsky mechanism [68].

The overall water splitting cell with NiCo-OH@Ni<sub>x</sub>Fe<sub>y</sub>O<sub>4</sub>/FF as anode and CoP@FeP/FF as cathode only requires 1.725 and 1.769 V to drive  $j_{500}$  and  $j_{1000}$  in 1 M KOH at 25 °C (Fig. 4a, b). In the conditions of industrial water splitting (6 M KOH at 60 °C), the driving voltage decreases to 1.558 V for  $j_{500}$  and 1.603 V for  $j_{1000}$ . At both experimental and industrial conditions, our cell shows lower voltage than that of commercial RuO<sub>2</sub> (+) || Pt/C (-) cell to drive  $j_{1000}$ . Moreover, the molar ratio of produced H<sub>2</sub> and O<sub>2</sub> is close to 2, and the Faraday efficiencies of H<sub>2</sub> and O<sub>2</sub> production calculated from Fig. 4c are 97.5% and 96.2% respectively, indicating the high efficiency of water splitting. In addition, as shown by chronopotentiometric measurement, the electrolytic cell exhibits excellent long-term stability in both common experimental condition (1 M KOH and 25 °C) and industrial condition (6 M KOH and 60 °C) (Fig. 4d, e). Specifically, the driving voltage only increased by 3.7% (1 M KOH and 25 °C) and 9.2% (6 M KOH and 60 °C) after 100 h operation at the industrial current density of 1000 mA cm<sup>-2</sup>. The water splitting performance of our cell is superior to most cells assembled by self-supported electrocatalysts (Fig. 4f and Table S6). The cell voltage of our cell (NiCo-OH@Ni<sub>x</sub>Fe<sub>y</sub>O<sub>4</sub>/FF || CoP@FeP/FF) at  $j_{1000}$  is slightly higher than that of (NiCo)<sub>3</sub>Ce<sub>4</sub> || (NiCo)<sub>3</sub>Ce<sub>4</sub> [69] and Ni<sub>0.8</sub>Fe<sub>0.2</sub>-AHNA || Ni nanowire array [70], because the cathodes in those cells have higher HER activity of our CoP@FeP/FF. But the fabrication of these cathodes is tedious and of high cost. Besides, the long-term stability of those cells cannot meet the expectation of FC HJU, whereas our cell can (Table S6). It is noteworthy that, under industrial condition, our water splitting cell outperforms the state-of-the-art cells (Table S7).

## 4. Conclusion

In summary, we constructed a self-supported NiCo-OH@Ni<sub>x</sub>Fe<sub>y</sub>O<sub>4</sub>/FF heterojunction catalyst for OER based on a two-step corrosion engineering. The catalyst only requires a small overpotential of 275 mV to drive a large current density of 1000 mA cm<sup>-2</sup> with excellent long-term stability. The superior catalytic performance is attributed to accelerated catalytic kinetics due to the electronic coupling at the heterojunction and rapid charge transfer to the current collector because of the intimate integration between the catalyst and the 3D conducting network. The overall water splitting cell equipped with NiCo-OH@Ni<sub>x</sub>Fe<sub>y</sub>O<sub>4</sub>/FF anode and CoP@FeP/FF cathode similarly constructed by corrosion engineering is able to drive 1000 mA cm<sup>-2</sup> at a low cell voltage of 1.769 V with excellent stability, promising for industrial application. Similar strategy can be applied to synthesize a variety of self-supported heterojunction catalysts by using different metal foams, corrosive metal salts, and reaction conditions (e.g., temperature, pH, solvent) for different catalytic applications.

## CRediT authorship contribution statement

**Zhong Li:** Investigation, Formal analysis, Writing – original draft, Visualization, Funding acquisition. **Xinglin Zhang:** Software, Formal analysis. **Zheyen Zhang:** Visualization, Writing – review & editing. **Peng Chen:** Methodology, Writing – review & editing. **Yizhou Zhang:** Validation, Supervision. **Xiaochen Dong:** Conceptualization, Resources.

## Declaration of Competing Interest

The authors declare no conflict of interest.

## Data Availability

Data will be made available on request.

## Acknowledgements

We would like to thank financial support by The International Postdoctoral Exchange Fellowship Program (No. PC2021035). The authors also would like to thank Shiyanjia lab for the DFT analysis ([www.shiyanjia.com](http://www.shiyanjia.com)).

## Appendix A. Supporting information

Supplementary data associated with this article can be found in the online version at [doi:10.1016/j.apcatb.2022.122311](https://doi.org/10.1016/j.apcatb.2022.122311).

## References

- [1] D. Zhu, M. Qiao, J. Liu, T. Tao, C. Guo, Engineering pristine 2D metal-organic framework nanosheets for electrocatalysis, *J. Mater. Chem. A* 8 (2020) 8143–8817, <https://doi.org/10.1039/d0ta03138k>.
- [2] F. Li, G. Han, H. Noh, Y. Lu, J. Xu, Y. Bu, Z. Fu, J. Baek, Construction of porous Mo<sub>3</sub>P/Mo nanobelts as catalysts for efficient water splitting, *Angew. Chem. Int. Ed.* 130 (2018) 14335–14339, <https://doi.org/10.1002/ange.201808844>.
- [3] Y. Li, L. Zhou, S. Guo, Noble metal-free electrocatalytic materials for water splitting in alkaline electrolyte, *EnergyChem* 3 (2021), 100053, <https://doi.org/10.1016/j.enerchem.2021.100053>.
- [4] M. Zhang, Q. Dai, H. Zheng, M. Chen, L. Dai, Novel MOF-derived Co@N-C bifunctional catalysts for highly efficient Zn-air batteries and water splitting, *Adv. Mater.* 30 (2018), 1705431, <https://doi.org/10.1002/adma.201705431>.
- [5] Q. Zhou, L. Liao, H. Zhou, D. Li, D. Tang, F. Yu, Innovative strategies in design of transition metal-based catalysts for large-current-density alkaline water/seawater electrolysis, *Mater. Today Phys.* 26 (2022), 100727, <https://doi.org/10.1016/j.mtphys.2022.100727>.
- [6] G. Zhang, Y. Li, X. Xiao, Y. Shan, Y. Bai, H. Xue, H. Pang, Z. Tian, Q. Xu, In situ anchoring polymetallic phosphide nanoparticles within porous prussian blue analogue nanocages for boosting oxygen evolution catalysis, *Nano Lett.* 21 (2021) 3016–3025, <https://doi.org/10.1021/acs.nanolett.1c00179>.
- [7] C. Wang, J. Li, Z. Zhou, Y. Pan, Z. Yu, Z. Pei, S. Zhao, L. Wei, Y. Chen, Rechargeable zinc-air batteries with neutral electrolytes: recent advances, challenges, and

prospects, *EnergyChem* 3 (2021), 100055, <https://doi.org/10.1016/j.chem.2021.100055>.

[8] F.T. Haase, A. Bergmann, T.E. Jones, J. Timoshenko, A. Herzog, H.S. Jeon, C. Rettenmaier, B.R. Cuenna, Size effects and active state formation of cobalt oxide nanoparticles during the oxygen evolution reaction, *Nat. Energy* 7 (2022) 765–773, <https://doi.org/10.1038/s41560-022-01083-w>.

[9] H. Yang, M. Driess, P.W. Menezes, Self-supported electrocatalysts for practical water electrolysis, *Adv. Energy Mater.* 11 (2021), 2102074, <https://doi.org/10.1002/aenm.202102074>.

[10] C. Liang, P. Zou, A. Nairan, Y. Zhang, J. Liu, K. Liu, S. Hu, F. Kang, H.J. Fan, C. Yang, Exceptional performance of hierachical Ni-Fe oxyhydroxide@NiFe alloy nanowire array electrocatalysts for large current density water splitting, *Energy Environ. Sci.* 13 (2020) 86–95, <https://doi.org/10.1039/C9EE02388G>.

[11] H. Sun, Z. Yan, F. Liu, W. Xu, F. Cheng, J. Chen, Self-supported transition-metal-based electrocatalysts for hydrogen and oxygen evolution, *Adv. Mater.* 32 (2019), 1806326, <https://doi.org/10.1002/adma.201806326>.

[12] L. Wu, L. Yu, X. Xiao, F. Zhang, S. Song, S. Chen, Z. Ren, Recent advances in self-supported layered double hydroxides for oxygen evolution reaction, *Research* 2020 (2020) 1–17, <https://doi.org/10.34133/2020/3976278>.

[13] X. Liu, M. Gong, S. Deng, T. Zhao, T. Shen, J. Zhang, D. Wang, Transforming damage into benefit: corrosion engineering enabled electrocatalysts for water splitting, *Adv. Funct. Mater.* 31 (2021), 2009032, <https://doi.org/10.1002/adfm.202009032>.

[14] C. Huang, Q. Zhou, D. Duan, L. Yu, W. Zhang, Z. Wang, J. Liu, B. Peng, P. An, J. Zhang, L. Li, J. Yu, Y. Yu, The rapid self-reconstruction of Fe-modified Ni hydroxysulfide for efficient and stable large-current-density water/seawater oxidation, *Energ. Environ. Sci.* 15 (2022) 4647–4658, <https://doi.org/10.1039/D2EE01478E>.

[15] Y. Bai, C. Liu, T. Chen, W. Li, S. Zheng, Y. Pi, Y. Luo, H. Pang, MXene-copper/cobalt hybrids via Lewis acidic molten salts etching for high performance symmetric supercapacitors, *Angew. Chem. Int. Ed.* 133 (2021) 25522–25526, <https://doi.org/10.1002/ange.202112381>.

[16] X. Liu, X. Guo, M. Gong, T. Zhao, J. Zhang, Y. Zhu, D. Wang, Regulated iron corrosion towards fabricating large-area self-supporting electrodes for an efficient oxygen evolution reaction, *J. Mater. Chem. A* 9 (2021) 23188–23198, <https://doi.org/10.1039/DITA06370G>.

[17] H. Zhou, F. Yu, Q. Zhu, J. Sun, F. Qin, L. Yu, J. Bao, Y. Yu, S. Chen, Z. Ren, Water splitting by electrolysis at high current densities under 1.6 volts, *Energy Environ. Sci.* 11 (2018) 2858–2864, <https://doi.org/10.1039/C8EE00927A>.

[18] C. Li, J. Hou, Z. Wu, K. Guo, D. Wang, T. Zhai, H. Li, Acid promoted Ni/NiO monolithic electrode for overall water splitting in alkaline medium, *Sci. China Mater.* 60 (2017) 918–928, <https://doi.org/10.1007/s04843-017-9089-y>.

[19] X. Xie, L. Du, L. Yan, S. Park, Y. Qiu, J. Sokolowski, W. Wang, Y. Shao, Oxygen evolution reaction in alkaline environment: material challenges and solutions, *Adv. Funct. Mater.* 32 (2022), 2110036, <https://doi.org/10.1002/adfm.202110036>.

[20] Y. Luo, Z. Zhang, M. Chhowalla, B. Liu, Recent advances in design of electrocatalysts for high-current-density water splitting, *Adv. Mater.* 34 (2022), 2108133, <https://doi.org/10.1002/adma.202108133>.

[21] J. Zhao, X. Li, G. Cui, X. Sun, Highly-active oxygen evolution electrocatalyzed by an Fe-doped NiCr<sub>2</sub>O<sub>4</sub> nanoparticle film, *Chem. Commun.* 54 (2018) 5462–5465, <https://doi.org/10.1039/C8CC02568A>.

[22] J. Chen, J. Chen, H. Cui, C. Wang, Electronic structure and crystalline phase dual modulation via anion-cation Co-doping for boosting oxygen evolution with long-term stability under large current density, *ACS Appl. Mater. Inter.* 11 (2019) 34819–34826, <https://doi.org/10.1021/acsm.9b08060>.

[23] W. Wang, Z. Wang, Y. Hu, Y. Liu, S. Chen, A potential-driven switch of activity promotion mode for the oxygen evolution reaction at Co<sub>3</sub>O<sub>4</sub>/NiO<sub>x</sub>H<sub>y</sub> interface, *eScience* 2 (2022) 438–444, <https://doi.org/10.1016/j.esci.2022.04.004>.

[24] X. Luo, P. Ji, P. Wang, R. Cheng, D. Chen, C. Lin, J. Zhang, J. He, Z. Shi, N. Li, S. Xiao, S. Mu, Interface engineering of hierarchical branched Mo-doped Ni<sub>3</sub>S<sub>2</sub>/Ni<sub>2</sub>P<sub>2</sub> hollow heterostructure nanorods for efficient overall water splitting, *Adv. Energy Mater.* 10 (2020), 1903891, <https://doi.org/10.1002/aenm.201903891>.

[25] B. You, M.T. Tang, C. Tsai, F. Abild-Pedersen, X. Zheng, H. Li, Enhancing electrocatalytic water splitting by strain engineering, *Adv. Mater.* 31 (2019), 1807001, <https://doi.org/10.1002/adma.201807001>.

[26] Z. Zhang, H. Wang, M. Ma, H. Liu, Z. Zhang, W. Zhou, H. Liu, Integrating NiMoO wafer as a heterogeneous ‘turbo’ for engineering robust Ru-based electrocatalyst for overall water splitting, *Chem. Eng. J.* 420 (2021), 127686, <https://doi.org/10.1016/j.cej.2020.127686>.

[27] H. Xu, H. Shang, C. Wang, Y. Du, Surface and interface engineering of noble-metal-free electrocatalysts for efficient overall water splitting, *Coord. Chem. Rev.* 418 (2020), 213374, <https://doi.org/10.1016/j.ccr.2020.213374>.

[28] X. Zhang, C. Liang, X. Qu, Y. Ren, J. Yin, W. Wang, M. Yang, W. Huang, X. Dong, Sandwich-structured Fe-Ni<sub>2</sub>P/MoS<sub>x</sub>/NF bifunctional electrocatalyst for overall water splitting, *Adv. Mater. Interfaces* 7 (2020), 1901926, <https://doi.org/10.1002/admi.201901926>.

[29] Y. Liu, X. Liang, L. Gu, Y. Zhang, G. Li, X. Zou, J. Chen, Corrosion engineering towards efficient oxygen evolution electrodes with stable catalytic activity for over 6000 h, *Nat. Commun.* 9 (2018), <https://doi.org/10.1038/s41467-018-05019-5>.

[30] Z. Zhang, X. Zhao, S. Xi, L. Zhang, Z. Chen, Z. Zeng, M. Huang, H. Yang, B. Liu, S. J. Pennycook, P. Chen, Atomically dispersed cobalt trifunctional electrocatalysts with tailored coordination environment for flexible rechargeable Zn-air battery and self-driven water splitting, *Adv. Energy Mater.* 10 (2020), 2002896, <https://doi.org/10.1002/aenm.202002896>.

[31] S. Wang, X. Li, Q. Yin, L. Zhu, Z. Luo, Highly active and selective Cu/SiO<sub>2</sub> catalysts prepared by the urea hydrolysis method in dimethyl oxalate hydrogenation, *Catal. Commun.* 12 (2011) 1246–1250, <https://doi.org/10.1016/j.catcom.2011.04.019>.

[32] R. Aladpoosh, M. Montazer, Functionalization of cellulose fibers alongside growth of 2D LDH platelets through urea hydrolysis inspired taro wettability, *Carbohydr. Polym.* 275 (2022), 118584, <https://doi.org/10.1016/j.carbpol.2021.118584>.

[33] D. Yu, L. Ge, B. Wu, L. Wu, H. Wang, T. Xu, Precisely tailoring ZIF-67 nanostructures from cobalt carbonate hydroxide nanowire arrays: toward high-performance battery-type electrodes, *J. Mater. Chem. A* 3 (2015) 16688–16694, <https://doi.org/10.1039/C5TA04509F>.

[34] H. Hu, B. Guan, B. Xia, X.W.D. Lou, Designed formation of Co<sub>3</sub>O<sub>4</sub>/NiCo<sub>2</sub>O<sub>4</sub> double-shelled nanocages with enhanced pseudocapacitive and electrocatalytic properties, *J. Am. Chem. Soc.* 137 (2015) 5590–5595, <https://doi.org/10.1021/jacs.5b02465>.

[35] K.H. Gayer, A.B. Garrett, The solubility of cobalt hydroxide, Co(OH)<sub>2</sub>, in solutions of hydrochloric acid and sodium hydroxide at 25°, *J. Am. Chem. Soc.* 72 (1950) 3921–3923, <https://doi.org/10.1021/ja01165a024>.

[36] K.H. Gayer, A.B. Garrett, The equilibria of nickel hydroxide, Ni(OH)<sub>2</sub>, in solutions of hydrochloric acid and sodium hydroxide at 25°, *J. Am. Chem. Soc.* 71 (1949) 2973–2975, <https://doi.org/10.1021/ja01177a008>.

[37] K. Porsch, A. Kappler, Fe<sup>II</sup> oxidation by molecular O<sub>2</sub> during HCl extraction, *Environ. Chem.* 8 (2011) 190, <https://doi.org/10.1071/EN10125>.

[38] S. Shariati, M. Faraji, Y. Yamini, A.A. Rajabi, Fe<sub>3</sub>O<sub>4</sub> magnetic nanoparticles modified with sodium dodecyl sulfate for removal of safranin O dye from aqueous solutions, *Desalination* 270 (2011) 160–165, <https://doi.org/10.1016/j.desal.2010.11.040>.

[39] W. Yang, J. Li, J. Yang, Y. Liu, Z. Xu, X. Sun, F. Wang, D.H.L. Ng, Biomass-derived hierarchically porous CoFe-LDH/CeO<sub>2</sub> hybrid with peroxidase-like activity for colorimetric sensing of H<sub>2</sub>O<sub>2</sub> and glucose, *J. Alloy. Compd.* 815 (2020), 152276, <https://doi.org/10.1016/j.jallcom.2019.152276>.

[40] L. Zheng, S. Wang, Y. Wang, Z. Zhao, P. Yang, J. Song, X. Shi, H. Zheng, Cooperative effect of bimetallic MOF-derived CoNi(OH)<sub>2</sub>@NiCo<sub>2</sub>S<sub>4</sub> nanocomposite electrocatalysts with boosted oxygen evolution activity, *Nanotechnology* 33 (2022), 265701, <https://doi.org/10.1088/1361-6528/ac5f99>.

[41] K. Ma, J.P. Cheng, J. Zhang, M. Li, F. Liu, X. Zhang, Dependence of Co/Fe ratios in Co-Fe layered double hydroxides on the structure and capacitive properties, *Electrochim. Acta* 198 (2016) 231–240, <https://doi.org/10.1016/j.electacta.2016.03.082>.

[42] Z. Lu, W. Xu, W. Zhu, Q. Yang, X. Lei, J. Liu, Y. Li, X. Sun, X. Duan, Three-dimensional NiFe layered double hydroxide film for high-efficiency oxygen evolution reaction, *Chem. Commun.* 50 (2014) 6479–6482, <https://doi.org/10.1039/C4CC01625D>.

[43] B. Dong, W. Liu, L. Chen, T. Zhang, Y. Fan, Y. Zhao, H. Li, W. Yang, Y. Sun, Unraveling the effect of chloride ion on the corrosion product film of Cr-Ni-containing steel in tropical marine atmospheric environment, *Corros. Sci.* 209 (2022), 110741, <https://doi.org/10.1016/j.corsci.2022.110741>.

[44] J. Hu, S. Li, J. Chu, S. Niu, J. Wang, Y. Du, Z. Li, X. Han, P. Xu, Understanding the phase-induced electrocatalytic oxygen evolution reaction activity on FeOOH nanostructures, *ACS Catal.* 9 (2019) 10705–10711, <https://doi.org/10.1021/acscatal.9b03876>.

[45] T. Nguyen, M. Fátima Montemor, γ-FeOOH and amorphous Ni-Mn hydroxide on carbon nanofoam paper electrodes for hybrid supercapacitors, *J. Mater. Chem. A* 6 (2018) 2612–2624, <https://doi.org/10.1039/C7TA05582J>.

[46] L. Lin, W. Ren, C. Wang, A.M. Asiri, J. Zhang, X. Wang, Crystalline carbon nitride semiconductors prepared at different temperatures for photocatalytic hydrogen production, *Appl. Catal. B: Environ.* 231 (2018) 234–241, <https://doi.org/10.1016/j.apcatb.2018.03.009>.

[47] M.S. Vidhya, G. Ravi, R. Yuvakkumar, D. Velauthapillai, M. Thambidurai, C. Dang, B. Saravanan, Nickel-cobalt hydroxide: a positive electrode for supercapacitor applications, *RSC Adv.* 10 (2020) 19410–19418, <https://doi.org/10.1039/d0ra01890b>.

[48] A. Ahlawat, V.G. Sathe, Raman study of NiFe<sub>2</sub>O<sub>4</sub> nanoparticles, bulk and films: effect of laser power, *J. Raman Spectrosc.* 42 (2011) 1087–1094, <https://doi.org/10.1002/jrs.2791>.

[49] S. Gao, Y. Cheng, M. Shirpour, Effects of cobalt deficiency on nickel-rich layered LiNi<sub>0.8</sub>Co<sub>0.1</sub>Mn<sub>0.1</sub>O<sub>2</sub> positive electrode materials for lithium-ion batteries, *ACS Appl. Mater. Inter.* 11 (2019) 982–989, <https://doi.org/10.1021/acsami.8b19349>.

[50] W. Zhu, W. Chen, H. Yu, Y. Zeng, F. Ming, H. Liang, Z. Wang, NiCo/NiCo-OH and NiFe/NiFe-OH core shell nanostructures for water splitting electrocatalysis at large currents, *Appl. Catal. B: Environ.* 278 (2020), 119326, <https://doi.org/10.1016/j.apcatb.2020.119326>.

[51] W. Li, X. Guo, P. Geng, M. Du, Q. Jing, X. Chen, G. Zhang, H. Li, Q. Xu, P. Braunstein, H. Pang, Rational design and general synthesis of multimetallic metal-organic framework nano-octahedra for enhanced Li-S battery, *Adv. Mater.* 33 (2021), 2105163, <https://doi.org/10.1002/adma.202105163>.

[52] Z. Wu, Y. Wang, Z. Xiong, Z. Ao, S. Pu, G. Yao, B. Lai, Core-shell magnetic Fe<sub>3</sub>O<sub>4</sub>@Zn/Co-ZIFs to activate peroxymonosulfate for highly efficient degradation of carbamazepine, *Appl. Catal. B: Environ.* 277 (2020), 119136, <https://doi.org/10.1016/j.apcatb.2020.119136>.

[53] Y. Liang, J. Wang, D. Liu, L. Wu, T. Li, S. Yan, Q. Fan, K. Zhu, Z. Zou, Ultrafast fenton-like reaction route to FeOOH/NiFe-LDH heterojunction electrode for efficient oxygen evolution reaction, *J. Mater. Chem. A* 9 (2021) 21785–21791, <https://doi.org/10.1038/DITA05136A>.

[54] X. Ren, T. Wu, Y. Sun, Y. Li, G. Xian, X. Liu, C. Shen, J. Gracia, H. Gao, H. Yang, Z. J. Xu, Spin-polarized oxygen evolution reaction under magnetic field, *Nat. Commun.* 12 (2021) 2608, <https://doi.org/10.1038/s41467-021-22865-y>.

[55] S.L. Zhang, B.Y. Guan, X.F. Lu, S. Xi, Y. Du, X.W.D. Lou, Metal atom-doped  $\text{Co}_3\text{O}_4$  hierarchical nanoplates for electrocatalytic oxygen evolution, *Adv. Mater.* 32 (2020), 2002235, <https://doi.org/10.1002/adma.202002235>.

[56] X. Li, Z. Kou, S. Xi, W. Zang, T. Yang, L. Zhang, J. Wang, Porous  $\text{NiCo}_2\text{S}_4/\text{FeOOH}$  nanowire arrays with rich sulfide/hydroxide interfaces enable high OER activity, *Nano Energy* 78 (2020), 105230, <https://doi.org/10.1016/j.nanoen.2020.105230>.

[57] L. Tan, J. Yu, C. Wang, H. Wang, X. Liu, H. Gao, L. Xin, D. Liu, W. Hou, T. Zhan, Partial sulfidation strategy to  $\text{NiFe-LDH}@\text{FeNi}_2\text{S}_4$  heterostructure enable high-performance water/seawater oxidation, *Adv. Funct. Mater.* 32 (2022), 2200951, <https://doi.org/10.1002/adfm.202200951>.

[58] Y. Zhang, P. Guo, S. Niu, J. Wu, W. Wang, B. Song, X. Wang, Z. Jiang, P. Xu, Magnetic field enhanced electrocatalytic oxygen evolution of  $\text{NiFe-LDH}/\text{Co}_3\text{O}_4$  p-n heterojunction supported on nickel foam, *Small Methods* 6 (2022), 2200084, <https://doi.org/10.1002/smtd.202200084>.

[59] P. Xiong, X. Zhang, H. Wan, S. Wang, Y. Zhao, J. Zhang, D. Zhou, W. Gao, R. Ma, T. Sasaki, G. Wang, Interface modulation of two-dimensional superlattices for efficient overall water splitting, *Nano Lett.* 19 (2019) 4518–4526, <https://doi.org/10.1021/acs.nanolett.9b01329>.

[60] J. Suntivich, K.J. May, H.A. Gasteiger, J.B. Goodenough, Y. Shao-Horn, A perovskite oxide optimized for oxygen evolution catalysis from molecular orbital principles, *Science* 334 (2011) 1383–1385, <https://doi.org/10.1126/science.1212858>.

[61] Y. Wang, C. Yang, Y. Huang, Z. Li, Z. Liang, G. Cao, Nickel induced electronic structural regulation of cobalt hydroxide for enhanced water oxidation, *J. Mater. Chem. A* 8 (2020) 6699–6708, <https://doi.org/10.1039/DOTA00010H>.

[62] Y. Huang, W. Chen, Z. Xiao, Z. Hu, Y. Lu, J. Chen, C. Chen, H. Lin, C. Chen, K. T. Arul, S. Wang, C. Dong, W. Chou, In situ/operando soft X-ray spectroscopic identification of a  $\text{Co}^{4+}$  intermediate in the oxygen evolution reaction of defective  $\text{Co}_3\text{O}_4$  nanosheets, *J. Phys. Chem. Lett.* 13 (2022) 8386–8396, <https://doi.org/10.1021/acs.jpcllett.2c01557>.

[63] J. Chen, H. Li, S. Chen, J. Fei, C. Liu, Z. Yu, K. Shin, Z. Liu, L. Song, G. Henkelman, L. Wei, Y. Chen, Co-Fe-Cr (oxy)hydroxides as efficient oxygen evolution reaction catalysts, *Adv. Energy Mater.* 11 (2021), 2003412, <https://doi.org/10.1002/aenm.202003412>.

[64] J. Zhang, H. Yang, B. Liu, Coordination engineering of single-atom catalysts for the oxygen reduction reaction: a review, *Adv. Energy Mater.* 11 (2021), 2002473, <https://doi.org/10.1002/aenm.202002473>.

[65] Y. Wen, J. Qi, P. Wei, X. Kang, X. Li, Design of  $\text{Ni}_3\text{N}/\text{Co}_2\text{N}$  heterojunctions for boosting electrocatalytic alkaline overall water splitting, *J. Mater. Chem. A* 9 (2021) 10260–10269, <https://doi.org/10.1039/DITA00885D>.

[66] P. Xiao, W. Chen, X. Wang, A review of phosphide-based materials for electrocatalytic hydrogen evolution, *Adv. Energy Mater.* 5 (2015), 1500985, <https://doi.org/10.1002/aenm.201500985>.

[67] J. Liu, Z. Wang, J. Li, L. Cao, Z. Lu, D. Zhu, Structure engineering of  $\text{MoS}_2$  via simultaneous oxygen and phosphorus incorporation for improved hydrogen evolution, *Small* 16 (2020), 1905738, <https://doi.org/10.1002/smll.201905738>.

[68] L. He, P. Cheng, C. Cheng, C. Huang, C. Hsieh, S. Lu,  $\text{Ni}_x\text{Fe}_y\text{Co}_{6-x-y}\text{Mo}_6\text{C}$  cuboids as outstanding bifunctional electrocatalysts for overall water splitting, *Appl. Catal. B: Environ.* 290 (2021), 120049, <https://doi.org/10.1016/j.apcatb.2021.120049>.

[69] J. Abed, S. Ahmadi, L. Laverdure, A. Abdellah, C.P. O'Brien, K. Cole, P. Sobrinho, D. Sinton, D. Higgins, N.J. Mosey, S.J. Thorpe, E.H. Sargent, In situ formation of nano Ni-Co oxyhydroxide enables water oxidation electrocatalysts durable at high current densities, *Adv. Mater.* 33 (2021), 2103812, <https://doi.org/10.1002/adma.202103812>.

[70] C. Liang, P. Zou, A. Nairan, Y. Zhang, J. Liu, K. Liu, S. Hu, F. Kang, H.J. Fan, C. Yang, Exceptional performance of hierarchical Ni-Fe oxyhydroxide@NiFe alloy nanowire array electrocatalysts for large current density water splitting, *Energy Environ. Sci.* 13 (2020) 86–95, <https://doi.org/10.1039/C9EE02388G>.